Tailoring Second-Harmonic Emission from (111)-GaAs Nanoantennas

Jürgen D. Sautter,[†,‡] Lei Xu,[¶] Andrey Miroshnichenko,[¶] Mykhaylo Lysevych,[§] Irina Volkovskaya,[‖] Daria A. Smirnova,[†] Rocio Camacho-Morales,[†] Khosro Zangeneh Kamali,[†] Fouad Karouta,[§] Kaushal Vora,[§] H. Hoe Tan,[§] Martti Kauranen,[⊥] Isabelle Staude,[‡] Chennupati Jagadish,[§] Dragomir N. Neshev,[*,†] and Mohsen Rahmani[†]

†*Nonlinear Physics Centre, Research School of Physics and Engineering, The Australian National University, Canberra, ACT 2601 Australia*

‡*Institute of Applied Physics, Abbe Center of Photonics, Friedrich Schiller University Jena, 07745 Jena, Germany*

¶*School of Engineering and Information Technology, University of New South Wales, Canberra, ACT 2600, Australia*

§*Department of Electronic Materials Engineering, Research School of Physics and Engineering, The Australian National University, Canberra, ACT 2601, Australia*

‖*Institute of Applied Physics, Russian Academy of Sciences, Nizhny Novgorod 603950, Russia*

⊥*Photonics Laboratory, Physics Unit, Tampere University, PO Box 692, FI-33014 Tampere University, Finland*

E-mail: Dragomir.Neshev@anu.edu.au

Abstract

Second-harmonic generation (SHG) in resonant dielectric Mie-scattering nanoparticles has been hailed as a powerful platform for nonlinear light sources. While bulk-SHG is suppressed in elemental semiconductors, e.g. silicon and germanium due to their centrosymmetry, the group of zincblende III-V compound semiconductors, especially (100)-grown AlGaAs and GaAs, have recently been presented as promising alternatives. However, major obstacles to push the technology towards practical applications are the limited control over directionality of the SH emission and especially zero forward/backward radiation, resulting from the peculiar nature of the second-order nonlinear susceptibility of this otherwise highly promising group of semiconductors. Furthermore, the generated SH signal for (100)-GaAs nanoparticles depends strongly on the polarization of the pump. In this work we provide both theoretically and experimentally a solution to these problems by presenting the first SHG nanoantennas made from (111)-GaAs embedded in a low index material. These nanoantennas show superior forward directionality compared to their (100)-counterparts. Most importantly, based on the special symmetry of the crystalline structure, it is possible to manipulate the SHG radiation pattern of the nanoantennas by changing the pump polarization without affecting the linear properties and the total nonlinear conversion efficiency, hence paving the way for efficient and flexible nonlinear beam shaping devices.

Keywords

Dielectric nanoantennas, second harmonic generation, III-V semiconductors, directional emission, Mie resonance, multipolar interference

Dielectric nanostructures have emerged as a promising building block for nanophotonic applications. The ability to control polarization, spectrum and phase of light or tailor radiation profiles at the nanoscale with very low losses in the near infrared (NIR) and visible regime compared to plasmonic nanostructures have attracted considerable attention in the photonics community.[1–7] Furthermore, optically induced electric and magnetic Mie-like resonances featured by dielectric nanoparticles which operate as optical nanoantennas, display tailorable near-field distributions and strong field enhancement inside the nanoantennas via the multipolar intereference effects, providing a promising route to improve the nonlinear conversion processes such as second/third harmonic generation (SHG/THG) at the nanoscale.[8–10]

For THG nanoantennas, silicon and germanium are often the material of choice due to their established fabrication and integration routines, as well as their high permittivity and third-order susceptibilities.,[8,11–18] For SHG however, the inversion symmetry needs to be broken rendering nanoparticles from these materials impractical. The class of III-V semiconductors with zincblende (ZB) crystal structure, like GaAs,[19,20] AlGaAs[21–24] and GaP[25] do not exhibit inversion symmetry and display SHG accordingly. While the losses for all these materials are negligible for frequencies below their respective bandgaps, GaAs is of particular interest as it features high permittivity and an unusually large second-order nonlinear susceptibility.[26,27] However, one major drawback of the ZB semiconductors is the peculiar form of the second-order nonlinear tensor $\chi^{(2)}_{ijk}$ that is commonly referred to as off-diagonal in the literature.

Here, we explain the implications of the second-order nonlinear tensors for SHG generation of nanoparticles fabricated from different wafer-cuts. A more thorough treatment of this topic can be found in the supporting information. First it should be noted, that for (100)-samples, the optical axis z of a pump beam impinging on a ZB crystal is aligned with the [100] crystal axis and hence the electric field lies in the respective plane, i.e. (100). As a result of the components of the $\chi^{(2)}_{ijk}$ tensor, the nonlinear currents are always parallel to the optical axis, resulting in zero SHG radiation along the optical axis at normal inci-

dence to (100)-samples. In nanoantennas, where optically induced near-fields can feature nonzero z-components, the SHG radiation along the optical axis is in principle possible even for (100)-samples. However, for the most common nanostructures such as disk, cuboid, the phase shift of the nonlinear currents induced in opposite halves of the antenna leads to destructive interference in the far-field resulting in typically "doughnut-shaped" radiation patterns,[21,28] that radiate most of the energy to the sides and with low directivity, thereby making it hard to collect the SHG signal using finite numerical aperture (NA) objectives.[20]

This is a considerable obstacle in the quest to implement nonlinear dielectric nanoantennas as practical light sources and as building blocks for nonlinear holograms.[29,30] In order to overcome this hurdle, the symmetry of the system needs to be reduced to shape the SH radiation into more suitable patterns with high directivity and with most of the energy radiating in a cone around the z-direction.

The reduction of the system symmetry can be achieved by tilting the pump beam[28,31,32] with respect to the main crystal axis or by reducing the symmetry of the nanoantennas and hence the resonant modes.[33] However, both of these alternatives come at the price of complexity in the nanoantenna design or experimental implementation. Recently, G. Marino et al.[34] have demonstrated that by normally incident pump polarized along various crystallographic axis of arrays of (100)-cut III-V nanoantennas, one can manipulate the direction of SH radiation. However, their technique is polarization-dependent and requires an arrays of nanoantennas. Here we present a novel approach in which the crystal axis and hence the nonlinear susceptibility tensor is rotated instead using GaAs nanonatennas fabricated from a (111)-cut wafer. Figure 1a displays the schematic of the single nanoantenna experiment. Cylindrical nanoantennas fabricated from a (111)-GaAs layer, as indicated in the inset of Figure 1 are excited by a focused laser beam and emit SH light. For the (100)-samples, the surface is terminated by one constituent of the III-V semiconductor. For (111)-samples, the tetrahedral bonding leads to one of the bonds pointing upwards and the three other bonds spreading out in a projected 120° angle (see inset in Figure 1a), leading

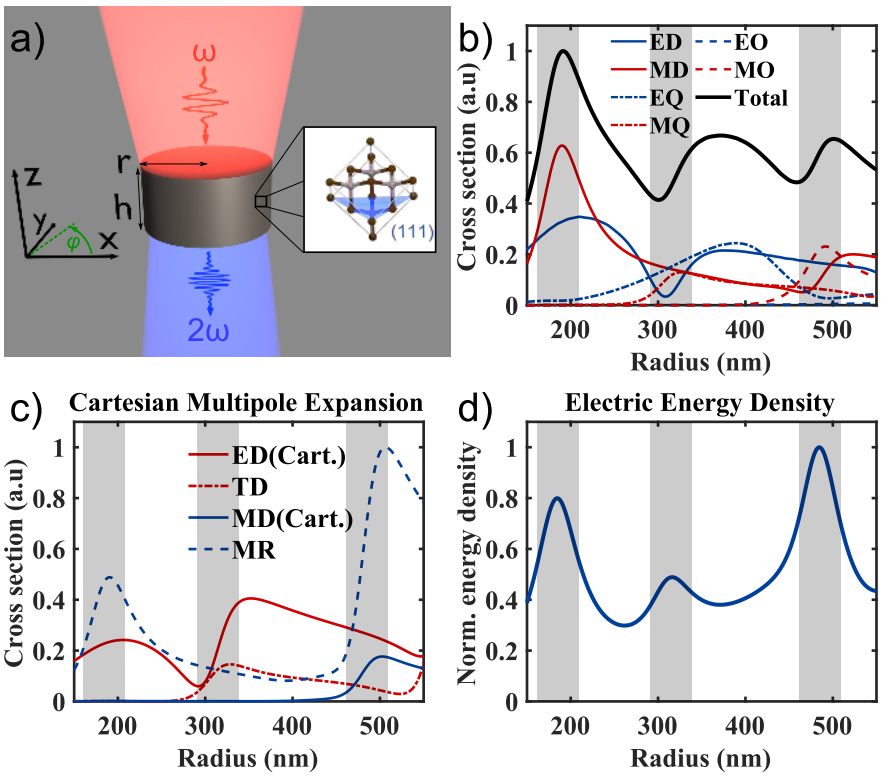

Figure 1: (a) Schematic of the single nanoantenna experiment. The inset shows the zincblende crystal structure in (111)-orientation, that is rotated with respect to the optical axis z (b) Calculated linear scattering cross section and spherical multipolar structure of a cylindrical GaAs nanoantenna with a height $h = 400\,\text{nm}$ and varying radii r under plane wave incidence at a wavelength of $\lambda = 1550\,\text{nm}$. (c) Calculated electric energy density inside the same nanoantenna with different disk radii. The grey bars in figures b-d highlight the three peaks in the electric energy density. (d) Calculated Cartesian multipole expansion of Cartesian electric and toroidal dipole modes, Cartesian magnetic dipole modes and mean radii distributions components.

to a three-fold symmetry. Despite these differences, the linear optical response of GaAs and that of the nanoantennas, is independent of the crystal orientation due to the isotropic refractive index of cubic crystal systems.

Figures 1b-d display the simulated linear scattering properties of cylindrical GaAs nanoantennas with a fixed height of 400 nm and varying radii excited by a plane wave at a wavelength of 1550 nm. All simulations shown in this work were performed employing the COMSOL Multiphysics® finite element method (FEM) solver. In Figure 1b, we show the scattering cross-section and perform multipolar decomposition using the polarization currents induced

inside the nanoantenna to study the nature of the resonances.[35] The three shaded wavelength ranges indicate peaks of the electric energy density inside the disk as shown in Figure 1c. They are of interest because enhanced SHG efficiencies can be expected from disks with near-field enhancement (the corresponding near-field distributions at these resonant positions can be seen in Figure S1 in the Supporting Information). The first peak of the energy density at around $r = 200\,\text{nm}$ corresponds to a maximum in the scattering cross section due to contributions from a magnetic dipole resonance. However, by comparing Fig. 1b and Fig. 1c, one can see that the enhancement of electric energy density inside the nanodisk at radii of $r = 315\,\text{nm}$ and $r = 480\,\text{nm}$ does not align with peaks in the scattering cross-section at these radii, while they coincide with the pronounced dips in the electric dipole and magnetic dipole excitations, respectively.

In order to gain physical insight into the second and third shaded wavelength ranges, we further perform Cartesian multipolar decomposition for both electric and magnetic dipole modes as shown in Figure 1d. The small peak in the energy density at r=315 nm coincides with an electric anapole state due to the overlap of Cartesian electric and toroidal dipole contributions. The far-field radiation from these current distributions cancels each other out, leading to a pronounced dip in the linear scattering cross section. The presence of an electric anapole state, as well as the excitations of magnetic dipole, electric and magnetic quadrupoles, result in an enhanced electric energy inside the nanoantennas. The energy density peak at 480 nm stems from the excitation of a magnetic anapole state associated with a magnetic octupole (MO) excitation (see Figure 1b). A strong Cartesian magnetic dipole moment is excited inside the disk, while its far-field distribution is significantly suppressed due to its interference with the mean radii (MR) distribution of the magnetic dipole. MR can be obtained as a third-order term in the expansion of the magnetic dipole moment and shares the same radiation pattern as the Cartesian magnetic dipole. Thus it is able to interfere with the Cartesian magnetic dipole and further cancel its scattering in the far-field.[36–38] This interference results in a strong near-field enhancement inside the nanodisk and further can

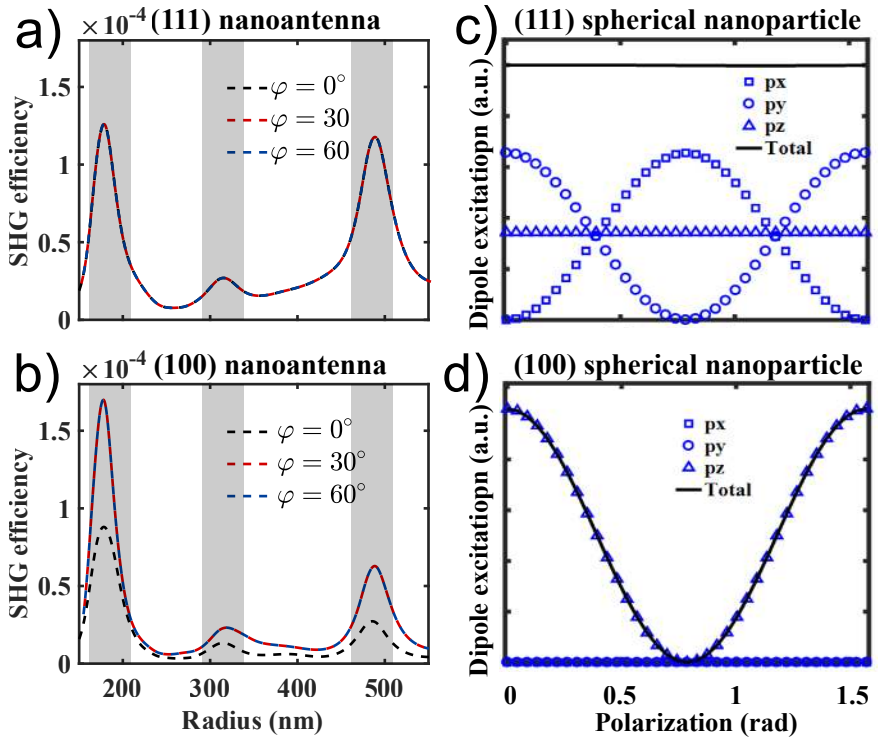

Figure 2: (a,b) Simulated total SHG generation efficiencies for (111)-and-(100)-oriented GaAs nanoantennas with parameters as in Figure 1 for varying pump polarization displaying polarization independence for the (111)-sample (c,d) Multipole expansion of nonlinear currents in a spherical dielectric nanoparticle.

be used to enhance the nonlinear process. Due to the isotropy of GaAs and the cylindrical symmetry of the nanoantennas, all quantities shown in Figure 1b-d are independent of the polarization of incident light and the crystalline orientation of the nanodisk.

In contrast to the linear response, the nonlinear response is not isotropic since the superposition principle does not apply, i.e. $\chi^{(2)}_{ijk}$ is not invariant under rotation. Hence the nonlinear response of antennas with different crystalline orientation differs considerably. Here, we demonstrate the importance of crystal orientation in the nonlinear regime. We show, that the SH far-field pattern can be controlled by the polarization of the fundamental wave, while the total nonlinear emission intensity stays constant due to the special properties of the nonlinearly generated multipoles of the harmonic emission stipulated by the specific nonlinear tensor elements of (111)-oriented material. The second-order susceptibility of ZB crystals has only three non-vanishing tensor components $\chi^{(2)}_{ijk}$ with $i \neq j \neq k \neq i$, where i, j, k refer

to the principal-axis system of the crystal, i.e. [100], [010] and [001]. In the following we consider a given electric field $\mathbf{E}$ (E_x, E_y, E_z) with ϕ being the angle between the in-plane component of electric field $E_\parallel(\omega) = \sqrt{|E_x|^2 + |E_y|^2}$ and x axis.

For (100) samples, where the principal crystal axes align with the global coordinate system, the resulting nonlinear currents can be written as:

$$\mathbf{J}_{100}(2\omega) = 4i\omega\varepsilon_0 d_{36} \begin{pmatrix} E_y(\omega)E_z(\omega) \\ E_x(\omega)E_z(\omega) \\ E_x(\omega)E_y(\omega) \end{pmatrix} = 4i\omega\varepsilon_0 d_{36} \begin{pmatrix} E_\parallel(\omega)E_z(\omega)\sin\varphi \\ E_\parallel(\omega)E_z(\omega)\cos\varphi \\ E_\parallel^2(\omega)\cos\varphi\sin\varphi \end{pmatrix} \tag{1}$$

by rewriting $E_x(\omega) = E_\parallel(\omega)\cos\varphi$ and $E_y(\omega) = E_\parallel(\omega)\sin\varphi$ and introducing $2d_{36}$, the value of the nonzero component of $\chi^{(2)}_{ijk}$. For (111)-crystals, the principal axis system is not aligned with the global coordinate system. Hence, in order to attain the nonlinear currents in the global coordinate system, the appropriate transformation (see supporting information for more details) needs to be employed resulting in:

$$\mathbf{J}_{111}(2\omega) = \begin{pmatrix} J_\parallel^\varphi(2\omega)\cos\varphi + J_\parallel^{2\varphi}(2\omega)\sin 2\varphi \\ J_\parallel^\varphi(2\omega)\sin\varphi + J_\parallel^{2\varphi}(2\omega)\cos 2\varphi \\ J_z(2\omega) \end{pmatrix} \tag{2}$$

where

$$J_\parallel^{2\varphi}(2\omega) = 2\sqrt{6}i\omega\varepsilon_0 d_{36} E_\parallel^2(\omega) \tag{3a}$$

$$J_\parallel^{\varphi}(2\omega) = -4\sqrt{3}i\omega\varepsilon_0 d_{36} E_\parallel(\omega)E_z(\omega) \tag{3b}$$

$$J_z(2\omega) = 2i\omega\varepsilon_0 d_{36}\left(2\sqrt{3}E_z^2(\omega) - \sqrt{6}E_\parallel^2(\omega)\right) \tag{3c}$$

It can be seen that for the given electric field $\mathbf{E}$ (E_x, E_y, E_z) with azimuthal angle φ with respect to the x axis, the in-plane components of the induced nonlinear current $J_\parallel^\varphi$ is oriented along φ, and $J_\parallel^{2\varphi}$ is oriented along $\pi/2 - 2\varphi$ with respect to x axis. Thus, if

the fundamental wave polarization is rotated by an angle ϕ in the transverse plane of the laboratory coordinate, the z-component of the generated nonlinear current $\mathbf{J}_z(2\omega)$ remains unchanged, wheres the in-plane component can be separated into two components that rotate by ϕ and -2ϕ when the exciting electric field is rotated by an angle ϕ, i.e., a rotation of 0 for $J_{\parallel}^{\varphi}$ and -3ϕ for $J_{\parallel}^{2\varphi}$ with respect to the pump polarization.

These two contributions to the nonlinear sources generate nonlinear multipoles with even $(J_z, J_{\parallel}^{2\varphi})$ and odd $(J_{\parallel}^{\varphi})$ value of the azimuthal number m respectively. Hence, they generate mutually-orthogonal multipolar currents at the second-harmonic (SH) frequency (see Section 2 and 3 in Supporting Information). Under rotation the amplitudes of the multipolar excitation coefficients do not change, therefore keeping the total SH conversion efficiency constant for varying pump polarization under normal incidence. It is subtle to see, that $\mathbf{J}^{\parallel}(2\omega)$ has threefold rotational symmetry with respect to the z-axis, i.e. the reference frame (the crystals [111]-axis), therefore correctly representing the corresponding crystal symmetry. As a result, by rotating the pump polarization by 120°, the excited nonlinear currents and hence the radiated far-field patterns are repeated.

In Figures 2a-b, we compare numerically the dependence of SH emission on the pump polarization φ from cylindrical (111)- and (100)-nanoantennas with the same parameters as before. It can be seen from Figures 2a-b, that the conversion efficiency depends on the pump polarization angle for (100)-nanoantennas, whereas it remains unchanged for (111)-oriented nanoantennas. As discussed above, this is due to the peculiar multipolar properties of the nonlinear currents generated in the nanoantennas which reveals that the amplitude with which different polar order l (dipole, quadrupole,...) are excited does not depend on the pump polarization. The corresponding far-field radiation however, varies due to φ-dependent amount with which different azimuthal orders m are excited within one polar order. This is a unique feature of (111)-nanoantennas for SHG, making it an advantageous platform for nonlinear wavefront shaping and nonlinear emission control.

To demonstrate this extraordinary property of (111)-ZB-nanoantennas, we proceed with

theoretical analysis of the SHG process in spherical GaAs nanoantennas of (111)- and (100)-orientation in single-mode approximation in Figure 2c, d. We can see for the (111)-sphere, that the z-oriented dipole component $a_e(1,0)$ is constant under variation of the FW polarization. The amplitude of the in-plane components $a_e(1,\pm1)$ alternate resulting with the predicted φ-dependance of the $J_{\parallel}^{2\varphi}$-component resulting in a constant total emission efficiency as predicted. In contrast, for the (100)-sphere, the total emission is strongly angle-dependent corresponding to the $\cos\varphi\sin\varphi$-dependance of $\mathbf{J_{100}}(2\omega)$ in equation 1.

In order to verify the predicted properties, we have fabricated and measured nanoantennas from (111)-GaAs. The fabrication steps are illustrated in Figure 3a. In order to examine the forward nonlinear directionality, it was crucial to accommodate GaAs nanoantennas on a glass substrate.[21] The first challenging step, not shown in the figures, was the process of growth of a thin (111)-GaAs layer on an aluminium arsenide (AlAs) buffer layer on a (111)-GaAs substrate using Metal-Organic Chemical Vapour Deposition (MOCVD). Although the epitaxial growth on (100)-GaAs substrates is a well-established process, planar growth on (111)-substrates is far from trivial.[39–42] Unlike (100)-substrates, (111)-substrates are either terminated with Ga or As atoms , labelled (111)A and (111)B respectively. Growth on (111)B-GaAs substrates requires high growth temperature and has a very narrow growth window with a rough morphology and high number of "hillocks".[40] Hence, to improve the surface morphology of the layers and to attain minimal surface roughness, we performed a growth optimization series to fine-tune the growth parameters of GaAs and AlAs (111)-layers with specular surfaces on (111)A-GaAs substrates. The films were grown on a (111)A-GaAs wafer in a showerhead type MOCVD reactor. First, 20 nm AlAs followed by 400 nm GaAs were deposited on a GaAs (111)A-wafer. The thin AlAs layer was used as an epitaxial lift-off layer. The deposition was carried out at 600 °C with a relatively low V/III ratio of 15. Trimethylgallium, trimethylaluminium and arsine were used as gallium, aluminum and arsenic precursors respectively. The nanoantennas were then fabricated by employing electron-beam lithography followed by a dedicated transfer procedure that we developed

earlier.[21] The structures were embedded in a benzocyclobutene (BCB) layer and subsequently transferred to a glass substrate (see Ref.[21] for a more detailed description of the transfer process).

This fabrication procedure offers several benefits as compared to conventional methods, where the nanostructures are placed on only a thin low-index layer. The low permittivity of the embedding polymer and the resulting index contrast lead to strong field confinement inside the nanoantenna. Furthermore, in contrast to prevailing designs where SHG is observed in reflection only[19,20,22,23,43,44] or alternatively in transmission by illumination through the substrate,[25] the glass substrate is not only transparent to the pump but also at the SH wavelength for an excitation wavelength of 1550 nm. This design allows for the optimization of the radiation in either transmission or reflection direction with excitation from free space or through the substrate, respectively. Additionally, the glass substrate does not generate SH that would otherwise interfere with the detection of the nanoantenna signal for (111)-wafers, a problem that does not occur for (100)-substrates since the bulk SHG in normal direction is zero for this configuration.

After fabrication, the sample was illuminated by a Toptica FemtoFiber Pro NIR femtosecond laser with a pulse length of 100 fs at a repetition rate of 80 MHz with a center wavelength of 1556 nm. The laser beam is focused on the GaAs nanoantennas using a NA = 0.7 NIR objective. The SH signal was collected in transmission using a NA=0.9 visible objective while the transmitted pump wave was filtered-out using a 800 nm short-pass filter (see Figure S3 - schematic of the nonlinear imaging setup in the Supporting Information). To compare the experimental SHG efficiency with the numerically predicted one, the laser peak power impinging on the geometric cross section of the nanoantennas was calculated and the SHG signal was evaluated using a calibrated camera.

Figure 3b displays the SHG conversion efficiencies $\eta = \frac{P_{\mathrm{SHG}}}{P_{pump}}$ for the (111)-GaAs nanoantennas for pump polarizations of $\varphi = 0°$, 30° and 60° at peak pump intensities of 1 GW cm^{-2}. As expected, the conversion efficiency is nearly equal for the different polarizations (see Fig-

ure S4 in the Supporting Information). The slight mismatch in resonance position as well as conversion efficiency can be explained by fabrication imperfections and the fact, that in experiments, only the light from a cone within an opening angle of 64° around the forward normal direction is collected by the objective. While maximum conversion efficiency was not the main goal of this work, the high percentage of the light collected in the experiment already leads to competitive conversion efficiency when compared to similar works.[19,22,43] (a comparison of the collection SHG emissions from (100)- and (111)-GaAs nanodisks can be seen in Figure S5 in the Supporting Information). In Figure 3c we analyze the scaling of the SHG signal for a disk of 340 nm, corresponding to the second peak in conversion efficiency, with the pump power. As expected, a quadratic scaling of the SHG power can be seen (see nonlinear signal presented in the inset of Figure 3c). Importantly, no saturation is observed for the highest available pump power. Therefore, even higher efficiencies could be obtained by increasing the illumination power. The measured conversion efficiency displays three distinct peaks that are visible for all three polarizations. Figure 3d shows the multipole expansion of the nonlinear currents for any pump polarization (see Figure S6 - the multipolar decomposotion of SHG in (100)-grown GaAs nanodisk in the Supporting Information for comparison). We note, that due to the relatively large size of the nanoantennas with respect to the SH wavelength, a multitude of multipole orders is present and we restrict ourselves to displaying the first four polar orders l, i.e. up to hexadecapoles. While the first two resonances display dominant electric octupolar character, the decomposition for the third resonance at 480 nm reveals similar-strength contributions from multiple orders (the measured and simulated back-focal-plane images can be seen in Figure S7 in the Supporting Information). We conclude that the peak in SH efficiency for these disk radii is mainly due to the strong field enhancement at the FW, as indicated by the grey regions corresponding to specific disk radius with strong field enhancement inside the nanoantennas.

Finally, the most intriguing feature of the nanoantennas is the capability to vary the radiation SH patterns at constant conversion efficiency and multipole character. Figure 4

displays the SHG radiated from a nanodisk of $r = 320\,\mathrm{nm}$ corresponding to an electric anapole mode (see also Figure 1). In experiments, we observe the corresponding peak at a radius of $r_{\mathrm{exp}} = 340\,\mathrm{nm}$ as determined by SEM micrographs. This nanoantenna features high directionality with a lobe centered close to the normal direction. Figure 4a displays the calculated SH radiation patterns of the disk under different pump polarization. Figure 4b shows the projection in forward-direction of this pattern, i.e the back-focal plane (BFP) image in the forward direction. The area inside the black circles corresponds to the light-cone visible through the collecting objective and therefore to the experimental BFP images displayed in Figure 4c. The imperfect agreement between experiment and simulation is likely due to a slight tilt of the nanoantennas embedded in BCB with respect to the substrate surface caused by tension within the BCB film that could happen during the transfer of the thin BCB layer onto a glass substrate. Due to three-fold rotational symmetry of the (111)-GaAs crystal with respect to the laboratory z-axis, in combination with the cylindrical symmetry of the nanoantennas, the nonlinear currents and hence the radiation patterns of the nanoantennas are identical under rotation of the disk by multiples of 60°. Conversely, if the polarization of the pump is rotated, the radiation patterns also repeat every 60° but rotated by 120°. Figure 4d displays the multipole expansion of the nonlinear currents for this nanoantenna. As explained above, it is exactly the same for all three, and indeed any, pump polarization. This feature is not only intriguing from a scientific point of view but also offers possible applications of polarization dependent beam steering or de-multiplexing at constant efficiency.

Conclusions

We have demonstrated theoretically and experimentally the first nonlinear GaAs nanoantennas with (111)-orientation situated on a glass substrate and compared their nonlinear optical properties with those of previously studied (100)-oriented nanoantennas. While the linear op-

tical properties of these nanoantennas are identical, we demonstrated a fundamental advantage in the nonlinear regime, where (111)-nanoantennas can emit non-zero nonlinear signal in forward/backward direction. Most importantly, this unique capability is accompanied with polarization-independent nonlinear conversion efficiencies. We theoretically demonstrated that employing (111)-oriented III-V semiconductor nanoantennas exhibit SHG conversion efficiencies independent of pump polarization associated with a constant magnitude of excited nonlinear currents with polar order l. However, the angle-dependence of azimuthal orders m of the excited multipolar currents with changing polarization leads to varying and rotating far-field radiation patterns The results presented here illustrate the great potential of (111)-oriented GaAs nanoantennas to emit second harmonic in forward direction, making them a viable platform for the next-generation photonic devices, including efficient nonlinear holograms and quantum-light sources.

Acknowledgements

J.S. and L.X. contributed equally to this work. The authors acknowledge the financial support by the Australian Research Council and the use of the Australian National Fabrication Facility (ANFF), the ACT Node. M.R. sincerely appreciates funding from ARC Discover Early Career Research Fellowship (DE170100250) and The Australian Nanotechnology Network. J.S. and I.S. gratefully acknowledge the financial support by the German Research Foundation (STA 1426/2-1). The work of A.E.M. was supported by a UNSW Scientia Fellowship. I.V. and D.S. acknowledge financial support by the Russian Foundation for Basic Research (Grants No. 18-02-00381, 19-02-00261). R.C.-M. acknowledges a grant from Consejo Nacional de Ciencia y Tecnología (CONACYT), Mexico. The work of M.K. was supported by the Flagship of Photonics Research and Innovation (Academy of Finland 320165) and by Tampere University.

References

(1) Novotny, L.; van Hulst, N. *Nature Photonics* **2011**, *5*, 83–90.

(2) Decker, M.; Staude, I. *Journal of Optics* **2016**, *18*, 103001.

(3) Kuznetsov, A. I.; Miroshnichenko, A. E.; Brongersma, M. L.; Kivshar, Y. S.; Luk'yanchuk, B. *Science* **2016**, *354*, aag2472.

(4) Rahmani, M.; Shorokhov, A. S.; Hopkins, B.; Miroshnichenko, A. E.; Shcherbakov, M. R.; Camacho-Morales, R.; Fedyanin, A. A.; Neshev, D. N.; Kivshar, Y. S. *ACS Photonics* **2017**, *4*, 454–461.

(5) Shcherbakov, M. R.; Liu, S.; Zubyuk, V. V.; Vaskin, A.; Vabishchevich, P. P.; Keeler, G.; Pertsch, T.; Dolgova, T. V.; Staude, I.; Brener, I.; Fedyanin, A. A. *Nature Communications* **2017**, *8*.

(6) Neshev, D.; Aharonovich, I. *Light: Science & Applications* **2018**, *7*.

(7) Zangeneh Kamali, K.; Xu, L.; Ward, J.; Wang, K.; Li, G.; Miroshnichenko, A. E.; Neshev, D.; Rahmani, M. *Small* 1805142.

(8) Shcherbakov, M. R.; Neshev, D. N.; Hopkins, B.; Shorokhov, A. S.; Staude, I.; Melik-Gaykazyan, E. V.; Decker, M.; Ezhov, A. A.; Miroshnichenko, A. E.; Brener, I.; Fedyanin, A. A.; Kivshar, Y. S. *Nano Letters* **2014**, *14*, 6488–6492.

(9) Carletti, L.; Locatelli, A.; Stepanenko, O.; Leo, G.; Angelis, C. D. *Optics Express* **2015**, *23*, 26544.

(10) Krasnok, A.; Tymchenko, M.; Alù, A. *Materials Today* **2018**, *21*, 8–21.

(11) Shcherbakov, M. R.; Shorokhov, A. S.; Neshev, D. N.; Hopkins, B.; Staude, I.; Melik-Gaykazyan, E. V.; Ezhov, A. A.; Miroshnichenko, A. E.; Brener, I.; Fedyanin, A. A.; Kivshar, Y. S. *ACS Photonics* **2015**, *2*, 578–582.

(12) Grinblat, G.; Li, Y.; Nielsen, M. P.; Oulton, R. F.; Maier, S. A. *ACS Nano* **2016**, *11*, 953–960.

(13) Grinblat, G.; Li, Y.; Nielsen, M. P.; Oulton, R. F.; Maier, S. A. *Nano Letters* **2016**, *16*, 4635–4640.

(14) Rahmani, M.; Xu, L.; Miroshnichenko, A. E.; Komar, A.; Camacho-Morales, R.; Chen, H.; Zárate, Y.; Kruk, S.; Zhang, G.; Neshev, D. N.; Kivshar, Y. S. *Advanced Functional Materials* **2017**, *27*, 1700580.

(15) Melik-Gaykazyan, E. V.; Shcherbakov, M. R.; Shorokhov, A. S.; Staude, I.; Brener, I.; Neshev, D. N.; Kivshar, Y. S.; Fedyanin, A. A. *Philosophical Transactions of the Royal Society A: Mathematical, Physical and Engineering Sciences* **2017**, *375*, 20160281.

(16) Xu, L.; Rahmani, M.; Kamali, K. Z.; Lamprianidis, A.; Ghirardini, L.; Sautter, J.; Camacho-Morales, R.; Chen, H.; Parry, M.; Staude, I.; Zhang, G.; Neshev, D.; Miroshnichenko, A. E. *Light: Science & Applications* **2018**, *7*.

(17) Nemati, A.; Wang, Q.; Hong, M.; Teng, J. *Opto-Electronic Advances* **2018**, *1*, 180009.

(18) Rahmani, M. et al. *Opto-Electronic Advances* **2018**, *1*, 180021.

(19) Liu, S.; Sinclair, M. B.; Saravi, S.; Keeler, G. A.; Yang, Y.; Reno, J.; Peake, G. M.; Setzpfandt, F.; Staude, I.; Pertsch, T.; Brener, I. *Nano Lett.* **2016**, *16*, 5426–5432.

(20) Löchner, F. J. F.; Fedotova, A. N.; Liu, S.; Keeler, G. A.; Peake, G. M.; Saravi, S.; Shcherbakov, M. R.; Burger, S.; Fedyanin, A. A.; Brener, I.; Pertsch, T.; Setzpfandt, F.; Staude, I. *ACS Photonics* **2018**, *5*, 1786–1793.

(21) Camacho-Morales, R. et al. *Nano Letters* **2016**, *16*, 7191–7197.

(22) Gili, V. F.; Carletti, L.; Locatelli, A.; Rocco, D.; Finazzi, M.; Ghirardini, L.; Favero, I.; Gomez, C.; Lemaître, A.; Celebrano, M.; Angelis, C. D.; Leo, G. *Optics Express* **2016**, *24*, 15965.

(23) Ghirardini, L.; Carletti, L.; Gili, V.; Pellegrini, G.; Duò, L.; Finazzi, M.; Rocco, D.; Locatelli, A.; Angelis, C. D.; Favero, I.; Ravaro, M.; Leo, G.; Lemaître, A.; Celebrano, M. *Optics Letters* **2017**, *42*, 559.

(24) Gili, V. F.; Carletti, L.; Chouchane, F.; Wang, G.; Ricolleau, C.; Rocco, D.; Lemaître, A.; Favero, I.; Ghirardini, L.; Finazzi, M.; Celebrano, M.; Angelis, C. D.; Leo, G. *Nanophotonics* **2017**, *7*.

(25) Cambiasso, J.; Grinblat, G.; Li, Y.; Rakovich, A.; Cortés, E.; Maier, S. A. *Nano Letters* **2017**, *17*, 1219–1225.

(26) Shoji, I.; Kondo, T.; Kitamoto, A.; Shirane, M.; Ito, R. *Journal of the Optical Society of America B* **1997**, *14*, 2268.

(27) Boyd, R. W. *Nonlinear Optics*; Elsevier LTD, Oxford, 2008.

(28) Carletti, L.; Locatelli, A.; Neshev, D.; Angelis, C. D. *ACS Photonics* **2016**, *3*, 1500–1507.

(29) Almeida, E.; Bitton, O.; Prior, Y. *Nature Communications* **2016**, *7*.

(30) Gao, Y.; Fan, Y.; Wang, Y.; Yang, W.; Song, Q.; Xiao, S. *Nano Letters* **2018**, *18*, 8054–8061.

(31) Xu, L.; Rahmani, M.; Smirnova, D.; Kamali, K. Z.; Zhang, G.; Neshev, D.; Miroshnichenko, A. *Photonics* **2018**, *5*, 29.

(32) Carletti, L.; Marino, G.; Ghirardini, L.; Gili, V. F.; Rocco, D.; Favero, I.; Locatelli, A.; Zayats, A. V.; Celebrano, M.; Finazzi, M.; Leo, G.; Angelis, C. D.; Neshev, D. N. *ACS Photonics* **2018**, *5*, 4386–4392.

(33) Ghirardini, L.; Marino, G.; Gili, V. F.; Favero, I.; Rocco, D.; Carletti, L.; Locatelli, A.; Angelis, C. D.; Finazzi, M.; Celebrano, M.; Neshev, D. N.; Leo, G. *Nano Letters* **2018**,

(34) Marino, G.; Gigli, C.; Rocco, D.; Lemaître, A.; Favero, I.; De Angelis, C.; Leo, G. *ACS Photonics* **2019**, *6*, 1226–1231.

(35) Grahn, P.; Shevchenko, A.; Kaivola, M. *New Journal of Physics* **2012**, *14*, 093033.

(36) Savinov, V.; Fedotov, V. A.; Zheludev, N. I. *Phys. Rev. B* **2014**, *89*, 205112.

(37) Paniagua-Domínguez, R.; Yu, Y. F.; Miroshnichenko, A. E.; Krivitsky, L. A.; Fu, Y. H.; Valuckas, V.; Gonzaga, L.; Toh, Y. T.; Kay, A. Y. S.; LukâĂŹyanchuk, B.; Kuznetsov, A. I. *Nature communications* **2016**, *7*, 10362.

(38) Luk'yanchuk, B.; Paniagua-Domínguez, R.; Kuznetsov, A. I.; Miroshnichenko, A. E.; Kivshar, Y. S. *Phys. Rev. A* **2017**, *95*, 063820.

(39) Reep, D.; Ghandhi, S. *Journal of Crystal Growth* **1983**, *61*, 449–457.

(40) Mayo, E.; Dickey, S.; Majerfeld, A.; Sanz-Hervás, A.; Kim, B. *Microelectronics Journal* **1997**, *28*, 727–734.

(41) Sanz-Hervás, A.; Cho, S.; Kim, J.; Majerfeld, A.; Villar, C.; Kim, B. *Journal of Crystal Growth* **1998**, *195*, 558–563.

(42) Cho, S.; Sanz-Hervás, A.; Kim, J.; Majerfeld, A.; Villar, C.; Kim, B. *Microelectronics Journal* **1999**, *30*, 455–459.

(43) Carletti, L.; Rocco, D.; Locatelli, A.; Angelis, C. D.; Gili, V. F.; Ravaro, M.; Favero, I.; Leo, G.; Finazzi, M.; Ghirardini, L.; Celebrano, M.; Marino, G.; Zayats, A. V. *Nanotechnology* **2017**, *28*, 114005.

(44) Vabishchevich, P. P.; Liu, S.; Sinclair, M. B.; Keeler, G. A.; Peake, G. M.; Brener, I. *ACS Photonics* **2018**, *5*, 1685–1690.

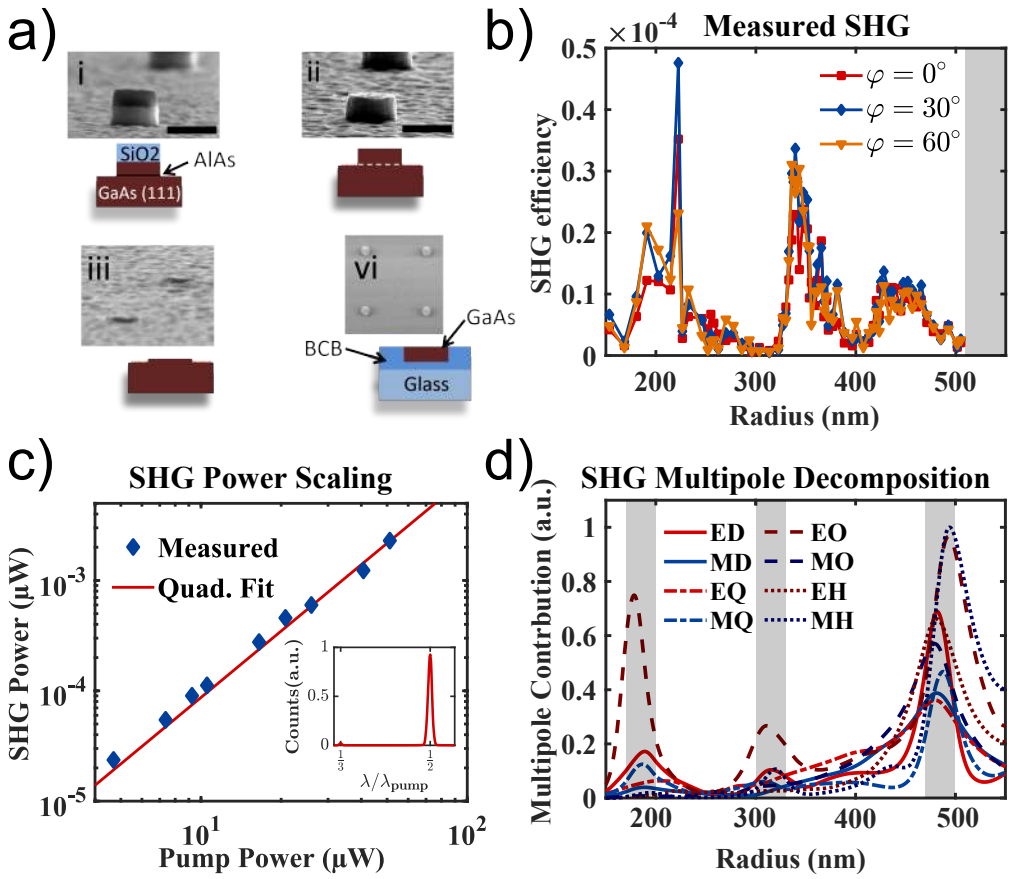

Figure 3: (a) Fabrication procedure, accompanied with SEM images, for the GaAs nanodisks in a transparent medium. (i) GaAs nanoantennas defined on a GaAs wafer via electron-beam lithography and sequential etching. SiO2 is used as a mask and AlAs as a sacrificial layer. (ii) removal of the SiO2 mask and AlAs buffer layer by HF acid, followed by coating of a BCB layer and curing. (iii) main substrate after removal of the GaAs over layer and (iv) final sample containing the GaAs antennas, after bonding and peeling off the AlGaAs nanoresonators. Scale bars are 1 μm. (b) Measured SHG efficiencies for cylindrical nanoantennas of varying radii and polarizations. (c) SHG power scaling with pump power displaying a quadratic dependence with a slope of two in the double logarithmic plot. The inset shows the spectrum of the nonlinear signal. (d) Multipole decomposition of SHG signal for all polarization directions.

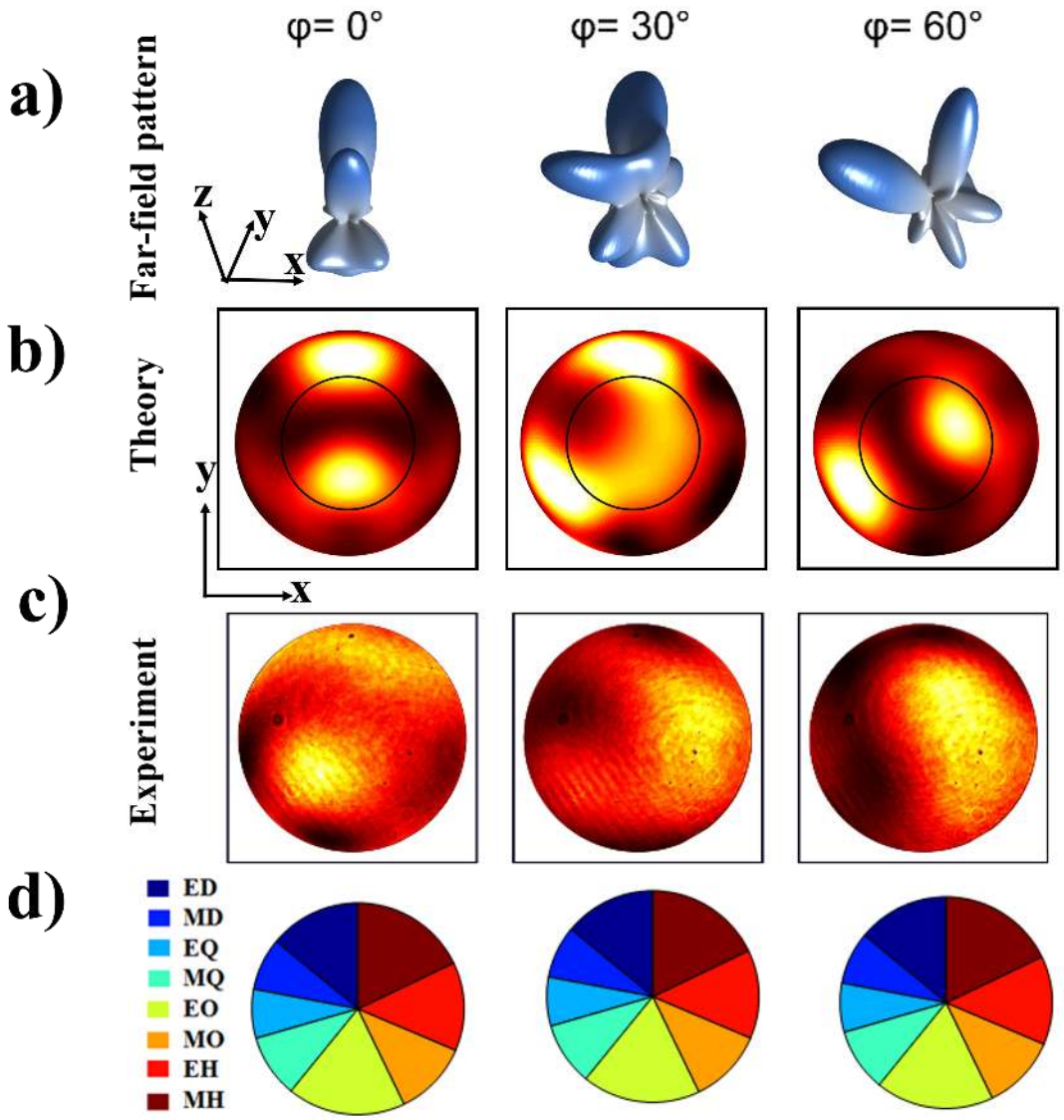

Figure 4: SHG from a (111)-GaAs nanodisk with h=400 nm and r=320 nm for pump polarizations of $\varphi = 0°$, $\varphi = 30°$ and $\varphi = 60°$. (a) Simulated radiation patterns. (b) Simulated and (c) measured back focal plane images in forward direction. The black circles in (b) show the angular range collected with a NA of 0.9 corresponding to the objective used in experiments. (d) multipole expansion of the nonlinear currents.